Development of Computer Aided Diagnosis Methods for Efficient Tuberculosis Detection

SYNOPSIS

Submitted in fulfilment of the requirements for the degree of

Doctor of Philosophy

In

Bioinformatics

By

ARUN CHAUHAN

Enrolment No. 106505

Under the supervision of

Dr. Chittaranjan Rout

DEPARTMENT OF BIOTECHNOLOGY AND BIOINFORMATICS

JAYPEE UNIVERSITY OF INFORMATION TECHNOLOGY

WAKNAGHAT, SOLAN-173234

INDIA

OCTOBER, 2015

Development of Computer Aided Diagnosis Methods for Efficient Tuberculosis Detection

Arun Chauhan

INTRODUCTION

Tuberculosis (TB) is a leading cause of morbidity and death worldwide. It is an infectious disease caused by the bacillus *Mycobacterium tuberculosis*, which affects mainly the lungs. It is contagious and airborne disease and ranks as the second leading cause of death from a single infectious agent, after the human immunodeficiency virus (HIV). The emergence of new drug resistant strains is beginning to exacerbate the problem, rendering the existing drugs ineffective, and necessitating determined action for any attempt to eradicate the disease. Nine million people fell ill with TB in 2013, including 1.1 million cases among people living with HIV. In 2013, 1.5 million people died from TB, including 3.6 lakhs HIV-positive persons. 5.1 lakhs women died from TB in the same year, including 1.8 lakhs HIV-positive women [1].

The new patients are generally assumed to have drug susceptible pulmonary TB, and are recommended six months of treatment by World Health Organization (WHO). The treatment consists of two phases: a two month intensive (treatment with Isoniazid, Rifampicin. Pyrazinamide and Ethambutol drugs) phase followed by a four month (treatment with Isoniazid and Rifampicin drugs) continuation phase [2]. The treatment of multi-drug resistant TB (MDR-TB) is more difficult. Mismanagement in treatment of drug susceptible TB often leads to drug resistant TB, like MDR, extensively drug-resistant (EDR) and totally drug-resistant (TDR). In hospitals, the disease is diagnosed on the basis of patient's symptoms, chest radiograph (CXR) and smear microscopy tests using Ziehl-Nelson staining (Figure 1). Although culture test and MTB/RIF are accurate but these tests are very costly and the former takes 4-8 weeks for results. Due to cost effectiveness, the ZN smear microscopy is usually the first bacteriological test for diagnosis of TB. Therefore, CXRs and ZN-stained microscopy remain the primary and rapid diagnostic tests for TB. Lack of resources and skilled radiologists particularly in rural areas of developing countries impedes effective diagnosis of TB from CXRs. A well-trained computer-aided diagnosis (CAD) method can assume the role

of a second CXR reader and may assist the radiologist in some facets of disease detection and decision making. The poor sensitivity of ZN smear microscopy is due to poorly trained staff, long working hours, human errors resulting from lack of concentration and tiredness, and analysis of very few view fields [3]. Better diagnosis of TB can only be achieved by developing more effective and efficient methods for interpretation of CXR and grading of bacilli in ZN-stained smear microscopy. Therefore, the CAD tools assume a lot of significance as they not only reduce diagnostic errors but also increase the efficiency in poor resource settings [3].

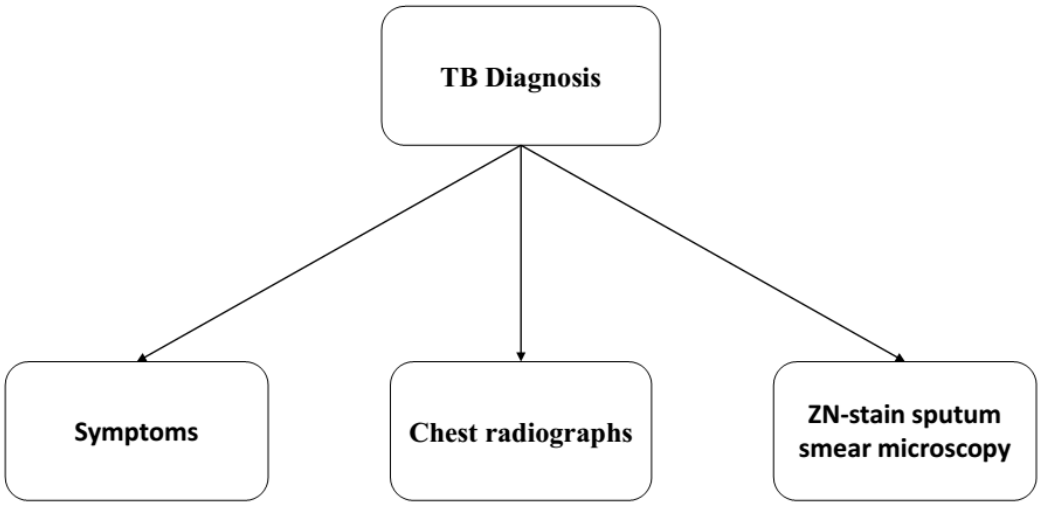

Figure 1. Diagnostic methods for TB detection in hospitals

The CAD system using CXRs

The success of the CAD methods in better diagnosis of breast cancer, colon cancer, lungs cancer, prostate cancer, coronary artery disease, congenital heart defects, etc., has suggested that TB may be detected more effectively by incorporating CAD methods [4-7]. A recent study has also shown that the performance of CXR readers in diagnosing TB can be improved with the support of CAD [8]. Though many CAD methods with reasonable accuracy were developed but those cannot be implemented into existing X-ray machine due to their dependency on segmentation.

CAD system using ZN-stained sputum smear slides

The examination of at least 100 view fields is required before reporting a smear microscopy result, but preferably examination of 300 view fields should be reported within 24 hours of collection of specimen [9]. Only 20 view fields are analyzed by the clinician in practice due

to time constraints. This may lead to lower efficiency of ZN staining in the diagnosis of TB. The other human errors may also occur due to lack of concentration and tiredness. This process takes about 20 minutes per sputum sample leading to delay in reporting results. The sensitivity is highly variable not only due to poorly trained staff but also the count of bacilli is very low in HIV infected people, old-age person and children. These problems may be solved by developing CAD systems for automated grading of the sputum smear slides. The automated grading requires the view fields to be focused, stitching of view fields into a single image, and then subsequently counting of the bacilli in an automated manner. If the CAD method can equal or exceed the performance of an experienced microscopist, it would reduce the number of patients requiring Xpert MTB/RIF or culture tests. With an endeavor to provide better healthcare, the followings are aims of the proposed work.

OBJECTIVES:

1. To evaluate the performance of methods extracting features from whole CXR images for classifying CXRs into TB and non-TB.
2. To develop a tool that can automatically classify a CXR into TB or non-TB without the need for segmentation. The tool can be implemented in X-ray machine for automatic detection of TB.
3. To develop a methodology for automated stitching of ZN-stained microscopy slide which can further be used for grading of the sputum smear slide.

OUTLINE OF SYNOPSIS

Our objectives were successfully accomplished by developing appropriate methodologies, and implementing those methods to develop Matlab toolbox which can automatically classify CXRs into TB or non-TB with high accuracy. The Matlab toolbox, TB-Xpredict, is available at http://sourceforge.net/projects/tbxpredict/ and is published in PLoS ONE journal. We have also developed method for automated stitching of ZN-view fields, which can further be used for automated grading of ZN-stained slides. The methods, results and discussion are described briefly chapterwise in the following sections with inclusion of necessary data in the form of figures and tables.

CHAPTER I. DEVELOPMENT OF CAD METHOD FOR THE DETECTION OF TB USING DIGITAL CXRs

The CAD techniques have been helpful in providing second opinion to the radiologists for their findings as well as assisting them in making their final decision regarding diagnosis with increased accuracy. Interpretation of CXRs is dependent on the expertise and skills of the radiologist, which is subject to human error. Even many district level hospitals in developing countries do not have skilled radiologists and incorrect diagnosis of TB takes place due to erroneous interpretation of CXR patterns. Although these techniques may by no means be able to achieve the level of cognitive ability and knowledge of a radiologist, nonetheless, a trained classifier can perform the prediction consistently without the intra-observer and inter-observer variability.

Basic methodology employed in most of the earlier reported CAD studies was segmentation and extraction of grey-level co-occurrence matrix (GLCM) textural features [10]. Ginneken *et al*. used the GLCM textural features on two datasets for classification of CXRs as TB or non-TB, but the performance of both varied significantly [11]. For one dataset, specificity of 90% was obtained while only 50% was achieved for the other. Detection of clavicle, and abnormalities in texture and shape in the CXRs were combined to develop a TB classification model by Hogeweg *et al* [12]. Semi-automated segmentation based classification model using textural features provided a prediction accuracy of 92.9% with sensitivity of 0.91 [13].

Current CAD methods employed for classification of CXR images are either object or region based [14-16]. These methods require segmentation and are prone to magnifying and carrying over low-level errors. The performance of GLCM features was inconsistent across various datasets [11], and these features lose significance when lungs have different shapes or CXRs have complex appearances due to overlapping of anatomical structures [13]. Commonly used manual or semi-automatic segmentation methods not only require high expertise but also make the classification model data and machine dependent. Although automated segmentation methods have potential to be used for development of CAD techniques, but studies have shown that automated segmentation of TB CXRs failed in many cases leading to incorrect classification [13]. Since context of the features obtained with respect to the whole image are expected to be more useful than local textural features, therefore, contextual scene based Gist features were used in this study for the prediction of TB from CXR [17]. Gabor [18], histogram of oriented gradients (HOG) [19], and pyramid histogram of oriented

gradients (PHOG) [20] features were also used in this study. The advantage with these methods is that they can be incorporated to X-ray machines for fully automated detection of TB. Localization of features was done through optimizing and fine-tuning various parameters, like region of interest (ROI), blocks and frequency range.

MATERIALS AND METHODS

Data collection

Two CXR digital image datasets were obtained from two different X-ray machines available at the National Institute of Tuberculosis and Respiratory Diseases (NITRD), New Delhi. These CXRs were taken in standard practice conditions followed by clinicians. In developing countries like India, the posterior-anterior (PA) CXRs are mostly taken while lateral CXRs are taken rarely. Therefore, only PA CXRs were used in the creation of the datasets. The CXRs were randomly collected over a period of one year with varied lung presentations. Dataset A (DA) was taken from Diagnox-4050 X-ray machine manufactured by Meditronics with CXRs digitized by AGFA CR35-X. Dataset B (DB) was obtained from PRORAD URS with Canon CXDI detectors. The tube voltage was set to 50 kV and 55kV for DA and DB respectively. E-7252X and E-7254X X-ray tubes manufactured by Toshiba, Japan were used by Diagnox-4050 and PRORAD URS respectively. Although AGFA CR35-X acquires 12-bit grayscale CXRs, but 8-bit CXRs (DA) were obtained due to imaging system used by the radiologists. 14-bit CXR digital images (DB) were obtained by using PRORAD URS. For both the datasets DA and DB, the acquired images were resized to 1024x1024 resolutions to obtain images with identical dimensions. No change in classification accuracy was noticed with respect to original sized images. CXRs from each dataset were randomly divided into training and test sets.

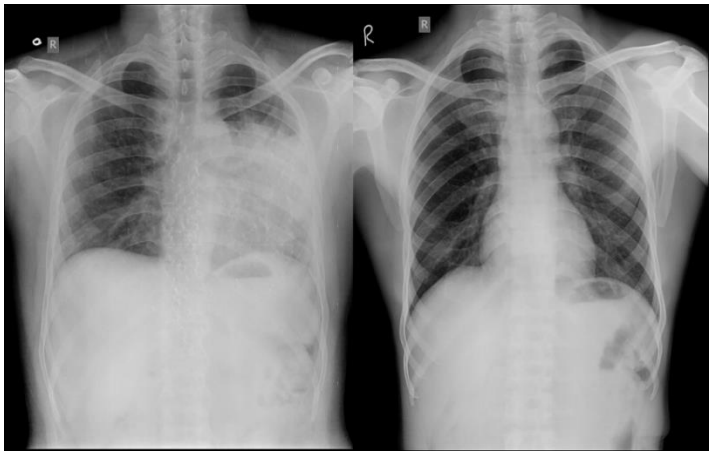

Figure 2. Left: CXR of TB patient, Right: CXR of normal person

DA comprised of training set (52 non-TB and 52 TB CXRs) and the independent test set (26 non-TB and 26 TB CXRs). Similarly, DB comprised of training set (50 non-TB and 50 TB CXRs) and the independent test set (25 non-TB and 25 TB CXRs). Selection of all non-TB and TB cases was based on the consensus of independent review of each CXR by two highly experienced chest radiologists from National Institute of Tuberculosis and Respiratory Diseases, New Delhi, India and Indira Gandhi Medical College, Shimla, India. The selection of abnormal CXRs, varying from subtle to severe TB findings, was based on radiological findings through the consensus of the radiologists. Datasets are available freely at http://sourceforge.net/projects/tbxpredict/files/data/.

Methodology

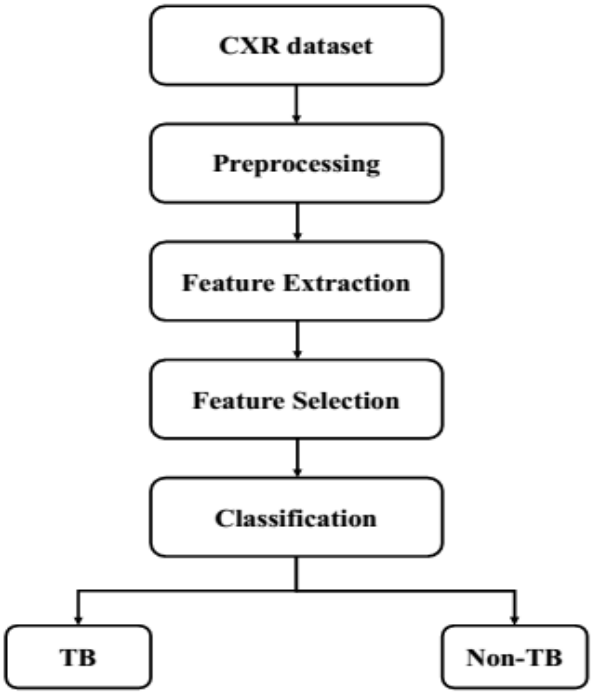

Figure 3: Flowchart depicting methodology for classification of CXRs as TB or Non-TB.

Segmentation

Segmentation is the process of dividing an image into a set of distinctive areas or regions that differ significantly qualitatively or quantitatively. It is a critical intermediate step in high level object-recognition tasks. Since existing methods required segmentation of CXRs, manual and automatic segmentation of CXRs for the dataset DA was done merely to evaluate the performance of reported segmentation method against the proposed method. Manual segmentation of CXRs was done with the help of ImageJ software [21]. To evaluate the

effectiveness of classification using features extracted from automated segmentation methods, Chan-Vese method [22] was used for the segmentation of CXRs from the dataset DA (Figure 4). Initial contour was developed using Euler-number [23] based segmentation with an auto-tuned threshold value as shown in Figure 4. The optimal threshold value for this segmentation is obtained on the basis of minimum and maximum values of the correlated image Euler numbers. Chan-Vese active contours segmentation was then used and the number of iterations for segmentation was fixed to 4000. The terminating criterion for segmentation does not depend on the gradient of the image.

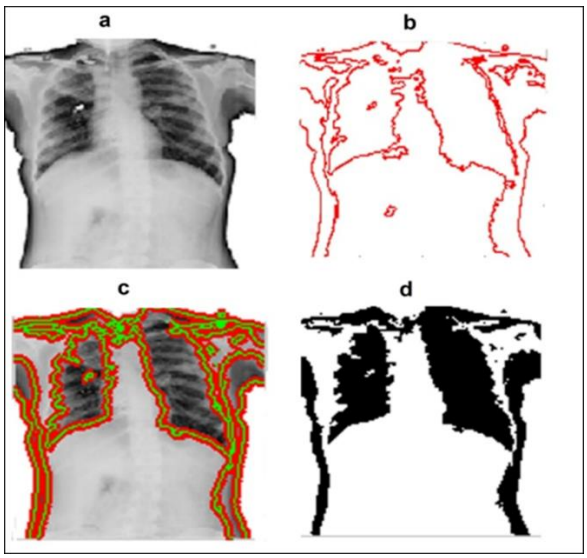

Figure 4. Chan-Vese active contour segmentation of a CXR. a. Original CXR image, b. Initial contour, c. Iterations for foreground segmentation, and d. Segmented image

Preprocessing

Preprocessing involves denoising of the image. Wavelet-based denoising is a well-known method in the field of digital image processing. Mean, Gaussian, anisotropic diffusion, Fourier transformation and the SURE orthonormal wavelet filters [24] were evaluated in this study for denoising of the images. Finally, orthonormal wavelet denoising of the image was used for this study as it provided best denoising effect with respect to visual inspection. The denoising process is parameterized as the sum of elementary non-linear processes with unknown weights. The estimate of mean square error (MSE) between denoised and clean image is minimized using Stein's unbiased risk estimate (SURE), a statistically unbiased estimate that depends only on the noisy image. The existence of this as a priori estimate avoids the requirement of statistical model for wavelet coefficients.

Feature Extraction

Textural (GLCM and Gabor) as well as other features, like Gist, HOG and PHOG were extracted from the digital CXRs. Details of the feature extraction methods used in this study are given below:

GLCM textural features

Textural features calculations are based on the statistical distribution of combinations of pixel intensities at specific positions relative to each other. The GLCM method extracts second-order statistics textural features. GLCM is a matrix with rows and columns equal to the number of grey levels. A two pixel offset (2,0 and 0,2) was used in this study.

Gabor features

Gabor filters have been found to be very effective in texture representation and discrimination [18, 25, 26]. These filters with different frequencies and orientations are used for extracting textural features from an image. The Gabor filters can be considered as edge detectors with adjustable orientations and scales. A self-similar filter dictionary is obtained by the association of rotation parameter, θ and scale factor, α with the Gabor function $g(x,y)$. Number of scales and orientations was set to six and ten respectively for creating feature vectors in this study. Frequency range was set between 0.01 and 0.4.

Gist features

These features are computed by convoluting the filter with an image at different scales and orientations. Thus, high and low frequency repetitive gradient directions of an image can be measured. The scores for filter convolution at each orientation and scale are used as Gist features for an image. These features are currently being used for scene classification [17, 27, 28]. Sixteen raw gist features are computed per feature map. 12 orientations per scale and 8 blocks were used for this study.

HOG features

This method was first introduced by Dalal and Trigg [19]. HOG breaks up a CXR image into small cells, computes the HOGs for each cell, normalizes HOGs using block pattern, and provides a descriptor for each cell [29]. In this study, block size and number of bins were set to 6x6 and 9 respectively. R-HOG was used as it provided better classification accuracy as compared to C-HOG.

PHOG features

These are spatial shape descriptors which describe an image by its spatial layout and local shape [20]. These descriptors are comprised of HOGs over each sub-region of an image at

each pyramid resolution level. In this study, the number of bins on histogram and number of pyramid levels at 360 degrees were set to 8 and 3 respectively.

Feature selection

Feature selection was performed using chi-square based method. Although several other feature selection methods such as correlation based feature selection, info gain and kernel principal component analysis were evaluated, but the performance of chi-square based feature selection method using WEKA software [30] was found to be the best with respect to classification results.

Classification

Support vector machines (SVMs) [31], a machine learning algorithm, is commonly used for classification and regression. Gaussian radial basis function was used in the study. LIBSVM [32], a supervised machine learning software, was used for labeling (classification) of a given CXR as TB or non-TB.

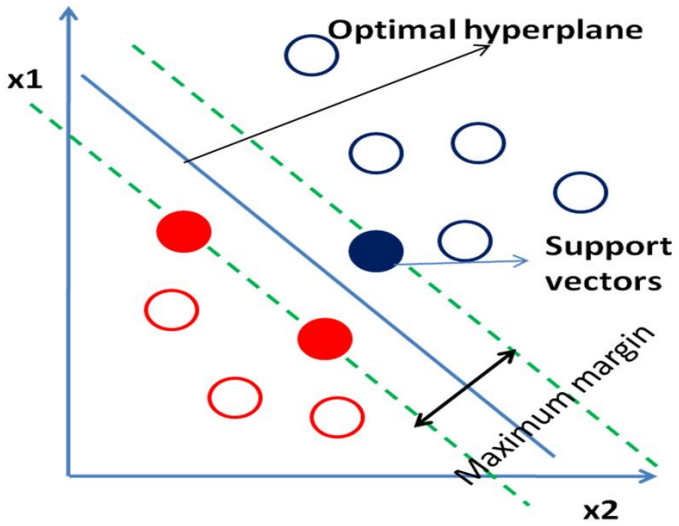

Figure 5: Hyperplane (blue line) representation in SVM. Red and blue circles represent data points from two different classes. Solid filled circles denote support vectors.

RESULTS AND DISCUSSION

Current CAD methods use local GLCM textural features extracted from segmented CXRs for the classification of CXRs. Segmentation is an important step for the effective extraction of

features. Implementation of CAD method into X-ray machines for the automatic prediction requires features to be extracted from automatically segmented or whole CXR images.

Performance of features extracted from automatically segmented CXRs

The performance of the GLCM textural features was quite low for the CXR dataset DA (Table 1). Prediction accuracy of only 65.4% was obtained for GLCM textural features extracted from automatically segmented CXRs, while 80.8% was obtained for manually segmented CXRs. The poor performance of automatic segmented CXRs may be attributed to severe intensity distortions [13], variability in lungs shape, and complex appearances of CXRs due to overlapping of anatomical structures.

Performance of features extracted from whole-CXR and manually segmented CXRs

Since low prediction accuracy was obtained using GLCM method, therefore, methods used to extract features from the whole image, like Gabor, Gist, HOG, and PHOG were evaluated for their ability to discriminate between the TB and non-TB CXRs. The Gabor, Gist, HOG, and PHOG features extracted from the whole CXR provided a prediction accuracy of 86.5%, 94.2%, 86.5%, and 92.3% respectively for dataset DA, and 92.0%, 86.0%, 86.0%, and 90% respectively for dataset DB (Table 1 and 2). The Gist features provided the maximum sensitivity of 0.961 for the dataset DA. This outcome is significant because sensitivity is considered as major criterion when measuring the effectiveness of a classification model for the detection of diseases. Although Gabor features provided comparable prediction accuracy to PHOG for dataset DB, but the latter provided significantly better 5-fold cross-validation accuracy of 86.6% in comparison to the former's 81.5%. Also, Gabor feature extraction is a computationally intensive process than PHOG method. For 5-fold cross-validation, the dataset were divided into five equal parts. One part was used for testing while the other four parts were used for the training of SVM. The procedure was repeated five times. The performance of features extracted from manually segmented images was comparable or lower than to those extracted from whole CXR image (Table 1). This may be attributed to the better spatial and contextual information provided by the whole CXR in comparison to the segmented one. Comparable performance between the whole and manually lung segmented CXRs indicated that these features (Gist, Gabor, HOG, and PHOG) were able to capture discriminative features without the need for segmentation of lungs (Table 1).

Table 1: Performance of classification of CXRs as TB or non-TB in dataset, DA using various feature extraction methods

Feature*	Accuracy	Sensitivity	Specificity	Precision	F-score	GMean	AUC	CI#	SE#
Gabor[1]	0.865	0.808	0.923	0.913	0.857	0.864	0.888	0.769-0.958	0.0482
Gab[2]	0.865	0.885	0.846	0.852	0.868	0.865	0.919	0.809-0.976	0.0392
Gab[3]	0.712	0.654	0.769	0.739	0.694	0.709	0.771	0.633-0.876	0.0668
Gist[1]	0.942	0.961	0.923	0.925	0.943	0.942	0.957	0.861-0.994	0.0301
Gist[2]	0.885	0.846	0.923	0.917	0.880	0.884	0.905	0.792-0.969	0.0444
Gist[3]	0.827	0.808	0.846	0.840	0.824	0.827	0.868	0.746-0.946	0.0497
HOG[1]	0.865	0.846	0.885	0.880	0.863	0.865	0.904	0.790-0.968	0.0456
HOG[2]	0.846	0.769	0.923	0.909	0.833	0.843	0.880	0.760-0.954	0.0483
HOG[3]	0.865	0.846	0.885	0.880	0.863	0.865	0.907	0.793-0.970	0.0440
PHOG[1]	0.923	0.885	0.962	0.958	0.920	0.922	0.956	0.859-0.993	0.0294
PHOG[2]	0.827	0.769	0.885	0.870	0.816	0.825	0.859	0.735-0.940	0.0520
PHOG[3]	0.808	0.846	0.769	0.786	0.815	0.807	0.828	0.698-0.919	0.0577
GLCM[2]	0.808	0.769	0.846	0.833	0.800	0.807	0.859	0.735-0.940	0.0510
GLCM[3]	0.654	0.769	0.538	0.625	0.690	0.644	0.623	0.478-0.753	0.0803

* Features extracted from: [1] indicates whole CXR, [2] indicates manually segmented CXR and [3] indicates automatic segmented CXR.

CI refers to confidence interval at 95% at P-value < 0.0001 whereas SE refers to standard error for AUC

Table 2: Performance of classification of CXRs as TB or non-TB in dataset, DB using various feature extraction methods

Feature*	Accuracy	Sensitivity	Specificity	Precision	F-score	GMean	AUC	CI#	SE#
Gab[1]	0.920	0.920	0.920	0.920	0.920	0.920	0.936	0.829- 0.986	0.0377
Gist[1]	0.860	0.880	0.840	0.846	0.863	0.860	0.893	0.773- 0.962	0.0520
HOG[1]	0.860	0.800	0.920	0.909	0.851	0.858	0.909	0.793- 0.972	0.0434
PHOG[1]	0.900	0.920	0.880	0.885	0.902	0.900	0.918	0.806- 0.977	0.0404

* Features extracted from: [1] indicates whole CXR, [2] indicates manually segmented CXR and [3] indicates automatic segmented CXR.

CI refers to confidence interval at 95% at P-value < 0.0001 whereas SE refers to standard error for AUC

Validation

The performance of various feature extraction methods used in this study is provided in Table 1 and 2. To validate the proposed methodology, five-fold cross validation and ROC curve analysis were done. PHOG features provided five-fold cross-validation accuracies of 83.2% and 86.6% for the datasets DA and DB respectively while 84.4% and 86.6% were obtained for the same datasets using Gist features. The AUC is a plot between true positive and false positive rates and it determines how well a model can distinguish between the TB and non-TB CXRs [33, 34].

Figure 6 shows high value of AUC for both Gist and PHOG features indicating a good discrimination between the TB and non-TB CXRs [33]. High AUC values were obtained (Table 1 and 2) at 95% confidence interval for our methods at P-level (AUC=0.5) smaller than 0.0001. Standard error (SE) of AUC was also calculated using the method of Delong *et al*. [35] and SE values were found to be quite low (Table 1 and 2). As inferred from the results of this study, the Gist and PHOG features were quite robust and provided better results without segmentation. These two features were implemented to develop TB-Xpredict, a MATLAB toolbox (Figure 7).

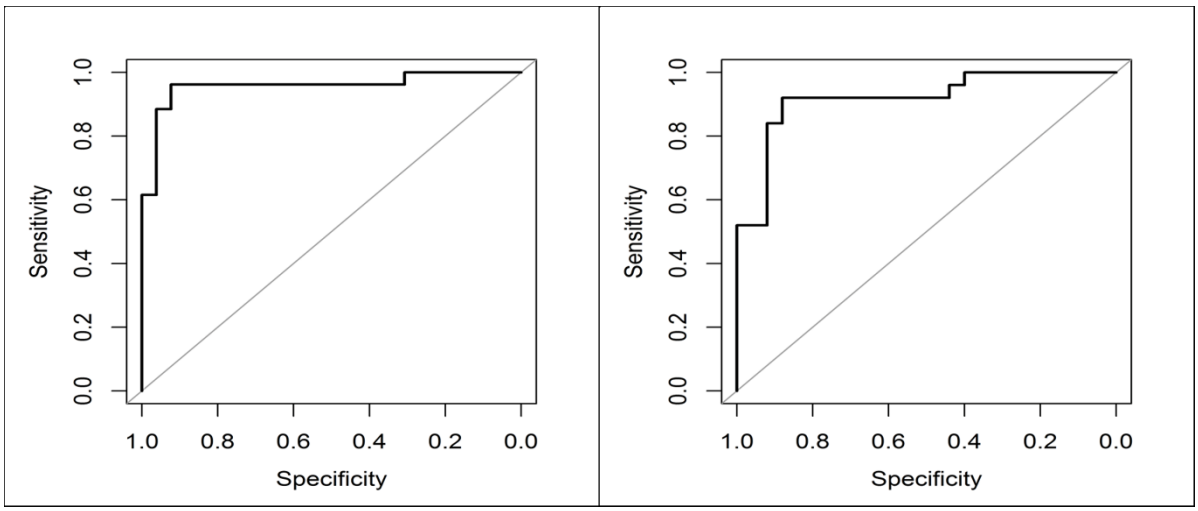

Figure 6. ROC plot for classification between TB and non-TB CXRs (DA) using Gist (left) and PHOG (right) features.

TB-Xpredict: MATLAB toolbox available at http://sourceforge.net/projects/tbxpredict/

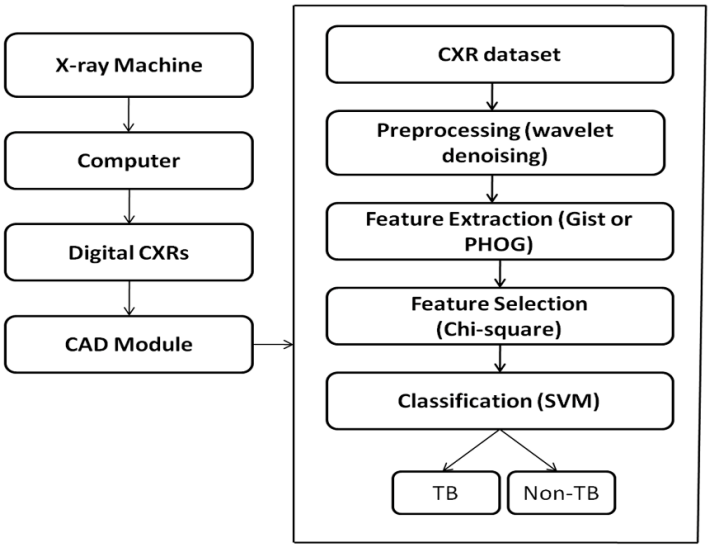

Figure 7. Workflow of TB-Xpredict Matlab toolbox

This toolbox has a user-friendly graphical user interface (GUI), which provides both training and prediction modules (Figure 8). The former enables the user to develop a model trained on his/her own CXRs (TB and non-TB CXRs) while the latter can be used for the classification of digital CXR(s). The user can independently upload CXRs into the prediction module to classify them using already trained model provided with the software. Training and prediction modules of the toolbox are available for Gist and PHOG features separately with the use of Gist as default. The toolbox automatically identifies the bit size and file format (dicom or jpeg) of the CXR images. The sample output of the toolbox ('PREDICT' module) is provided in Figure 9.

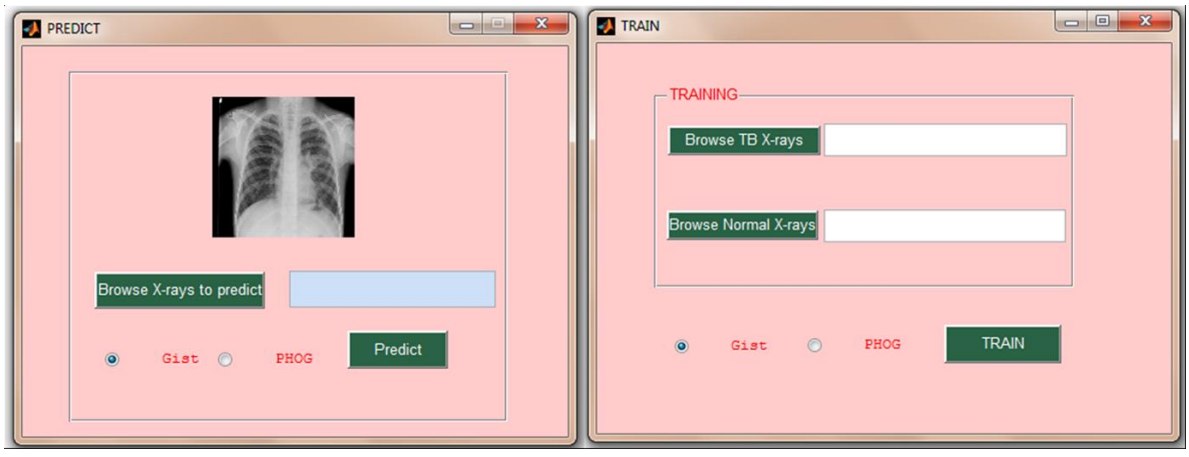

Figure 8: GUI of Prediction (PREDICT) and Training (TRAIN) Modules in TB-Xpredict.

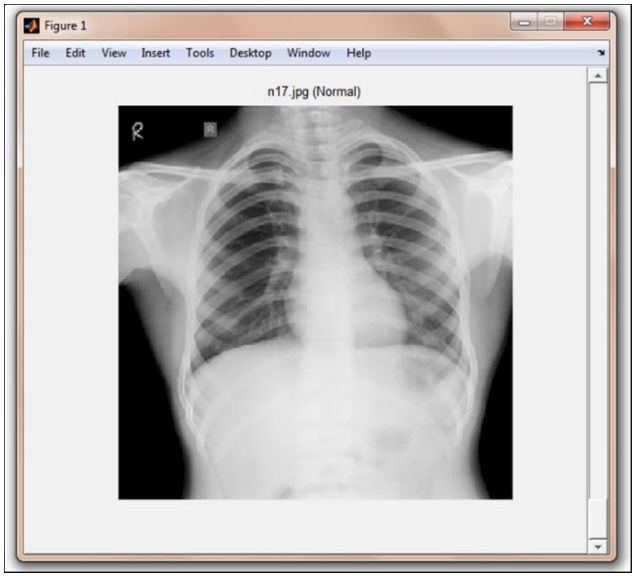

Figure 9: GUI of sample output provided by TB-Xpredict

Since TB-Xpredict does not require prior segmentation of digital CXR images, this toolbox can easily be incorporated into existing X-ray machines for the automated classification of CXR as TB or non-TB. X-ray machines with such modules can effectively be used for the mass screening of TB in high-burden areas. GUI of TB-Xpredict enables user to train and classify CXRs without the need of expertise in image processing. User only needs to upload positive and negative CXRs separately, and the module trains the model in an automatic manner. The newly developed model can be used for the prediction of CXRs using prediction module. Since illumination and other parameters do not differ significantly in test data with respect to training model, automated prediction methods which use CXRs from the same X-ray machine for training as well as classification generally may lead to better prediction accuracy. Furthermore, such model may become more efficient as the number and diversity of training data increases over time.

CHAPTER II: AUTO-STITCHING OF ZN-STAINED MICROSCOPY VIEW FIELDS

Automated stitching is likely to increase the number of view fields (Figure 10) to be analyzed by forming mosaic. The slide can be graded as TB or non-TB by using automated detection of bacilli. Hence the computer-aided diagnosis (CAD) methods have potential to reduce human errors in diagnosis. If the CAD-assisted ZN-stained microscopy for TB detection can equal or exceed the performance of an experienced microscopist then the sensitivity of this test is likely to increase. The methods for automatic identification of bacilli in view fields have been developed by Sadaphal *et al.* [37], Veropoulos *et al.* [3], Khutlang *et al.* [38] and Somoskövi *et al.* [9]. Forero-Vargas [39] has developed segmentation and autofocusing techniques for TB microscopy images. Mateos-Pérez *et al.* [40], Russell and Douglas [41], and Costa Filho *et al.* [42] have developed and compared methods related to autofocusing of TB microscopy images. Patel and Douglas have developed method for microscope auto-positioning, so as to automatically bring desired fields to the field-of-view of the microscope [55]. But, before the slides are graded, the overlapping view fields obtained should be stitched together to form one final mosaic on which further image processing techniques can be applied for counting bacilli. In this proposed work, a method has been developed for automated stitching of the various view fields into one final mosaic which can be used for automated grading of the smear slide.

Many studies have been performed for image stitching which use Harris Corner detection [43], scale invariant feature transform (SIFT) feature extraction [44-46] and speeded up robust feature (SURF) feature extraction [47] algorithms for extracting feature points. MicroMos, an open-source tool, can be used to build mosaics from microscopy view field images [48]. Autostitch, well-known software for building panorama, uses SIFT features extraction for image stitching [46]. TBDx, an auramine-stained fluorescence smear microscopy system, has shown promising results. This instrument is capable of loading of slides onto a microscope, focusing and digital capturing of images in an automated manner, and then classifying the sputum smear as positive or negative TB using image processing techniques [36]. Since view fields are acquired in a row fashion (Figure 11), divide and conquer strategy was implemented to reduce computational time. SIFT [49] method was used for feature detection and extraction followed by outlier removal using random sample consensus (RANSAC) [50]. SURF was not used since extracting features by this algorithm is not robust to the changes of viewpoints [51]. The view field was cropped into subparts which

were then stitched together. To validate the stitching method, the stitched view fields and the original images were then compared visually as well as quantitatively to evaluate the effectiveness of the method.

MATERIALS AND METHODS

Collection of data for stitching view fields

Two datasets were acquired from Indira Gandhi Medical College, Shimla using Labomed Digi 3 digital microscope which features Lx400 trinocular microscope and an iVu 5100 digital camera module 5.0 megapixel CMOS sensor. The images acquired were of dimension of 800x600 pixels with bit depth of 24 and resolution of 120 dpi at 100x magnification. Dataset DA and DB containing overlapping view fields comprised of 50 images each obtained from two different ZN-stained slides. The directions in which digital images of the view fields were acquired from sputum smear slide are shown in Figure 11. The digital image of the each view field was divided into different overlapping subparts ((2x2 (P1), 3x3 (P2) and (3x5 (P3)) of equal sizes, so as to mimic the images obtained from an automated motorized microscope.

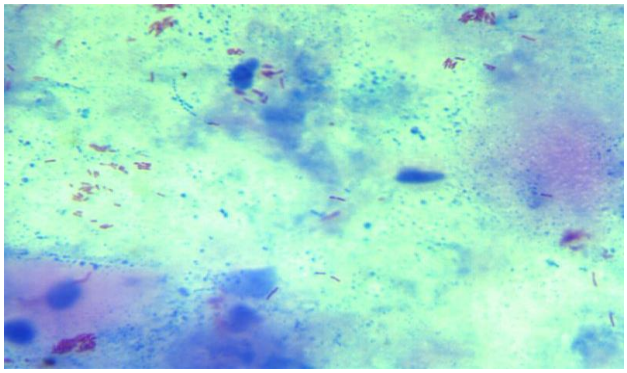

Figure 10. Digital image of the view field of ZN-stained sputum smear slide. The red elliptical objects are the *Mycobacterium tuberculosis* bacilli.

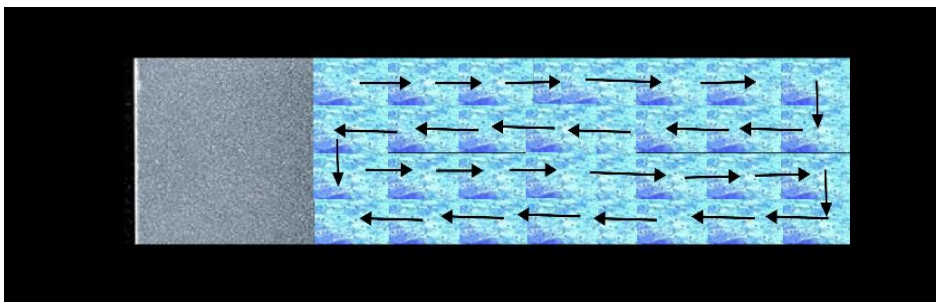

Figure 11: Depiction of view fields in a ZN-stained sputum smear slide and direction in which they are acquired.

METHODOLOGY

The flow diagram of methodology used to stitch subparts of view field is provided in Figure 12.

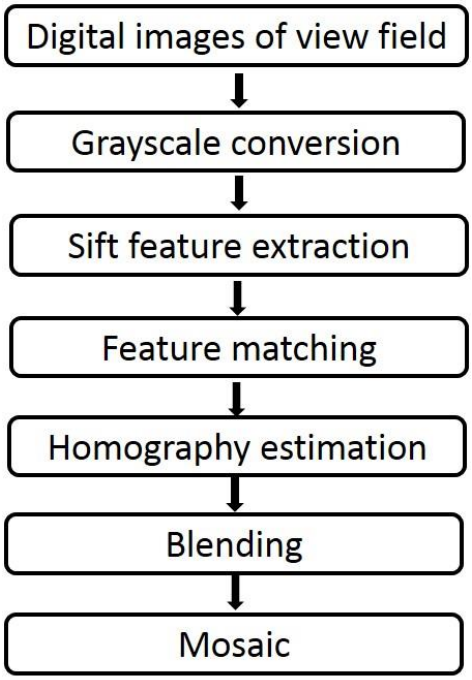

Figure 12. Flow diagram of methodologies implemented in auto-stitching method

The autostitching of image was done using following steps:

Conversion to grayscale image:

The color image was converted to grayscale by conversion of image from RGB to HSV colorspace followed by separation into its three different components H, S and V. A color space is a representation of color in a reproducible manner. Almost all color management software use a device-independent space defined by the Commission International de l' éclairage (CIE). CIE XYZ (1931), CIE L*A*B* and CIE L*U*V* are the common forms in which the CIE space of visible color is expressed. Although, they contain the same colors, but the distribution of the colors is different. CIELAB or CIEXYZ is the reference standards for defining a color space. The former is based on one channel for Luminance (L) and two color channels (‘a’ and ‘b’), and is the most complete color model to describe all the colors visible to human eye. The HSV (hue (H), **s**aturation (S), value (V)) is a transformation of a RGB colorspace and commonly used color space in image processing.

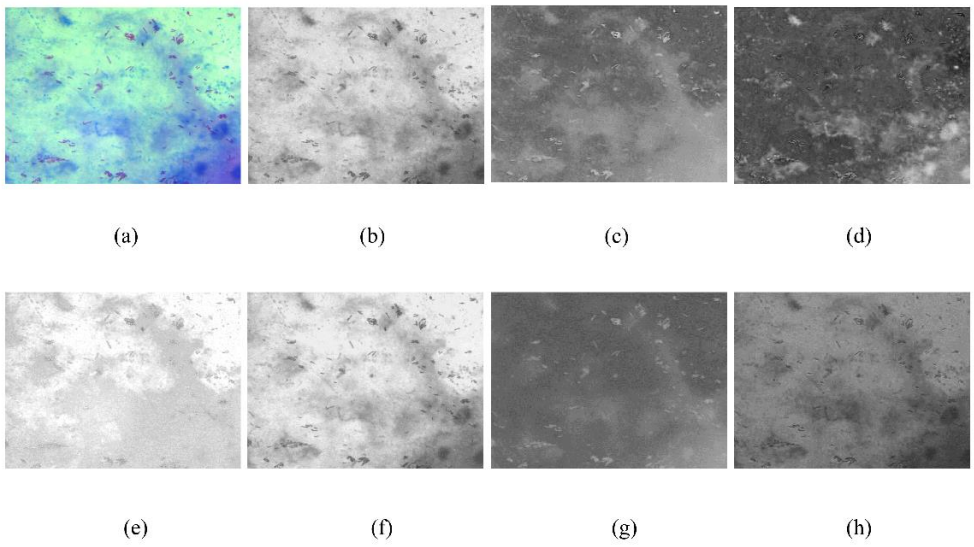

Figure 13. ZN smear slide view field image and its transformation in different colorspace. (a) Original RGB image, (b) H channel, (c) S channel, (d) V channel, (e) L channel, (f) a channel, (g) b channel, and (h) Grayscale image obtained by retaining only luminance.

Feature detection and extraction

SIFT features were then extracted using grayscale image. The invariant descriptor is computed by combining local gradients in orientation histograms allowing edges to shift slightly without changing the descriptors, giving some robustness to affine change. Invariance to illumination is achieved by normalizing the descriptors and using gradients [26]. Our method can handle images with varying illumination and orientation, since SIFT features are invariant under rotation and scale changes.

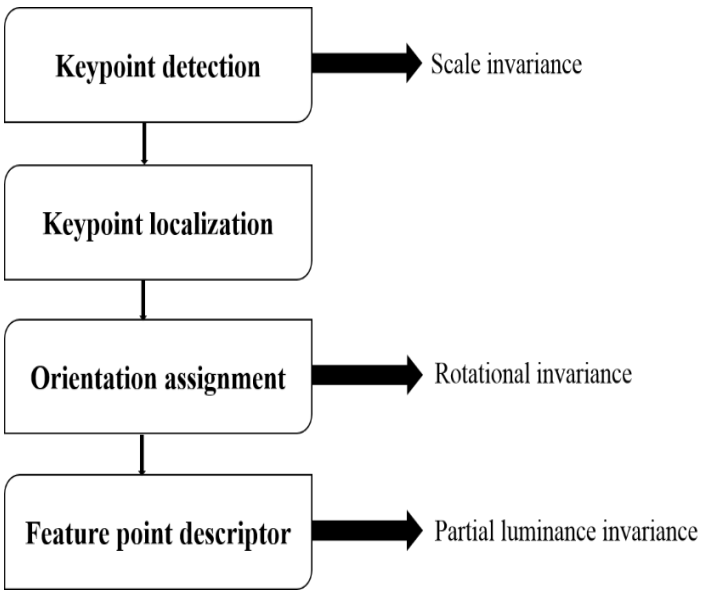

Figure 14. Flowchart of SIFT descriptor extraction

In this method, the image is transformed into scale-invariant coordinates with respect to local features. It comprises of four major steps: keypoint detection, keypoint localization, orientation assignment, and key point descriptor.

i) Keypoint Detection:

The potential interest points that are invariant to scale and orientation are searched over scale space using a difference of Gaussian (DoG) function.

ii) Keypoint Localization

The potential keypoints are then accurately localized by rejecting those with low contrast or are poorly localized along an edge.

iii) Orientation Assignment

Consistent orientation is assigned to each keypoint based on local image properties, and therefore, invariance to image rotation is attained. The gradient orientations of points within a region surrounding the keypoint are used to form the orientation histogram which covers the 360 degree range of orientations with 36 bins. Dominant directions of local gradients are indicated by the peaks in the orientation histogram. Multiple keypoints are generated at the same location and scale but with different orientations for locations with multiple peaks of similar magnitude.

iv) Feature point descriptor

At each image sample point near feature point location, gradient magnitude and orientation are computed for creating a feature descriptor. These descriptors are then weighted by a Gaussian window.

Matching

The best match for each keypoint in the template image is found by recognizing its nearest neighbor in the database of keypoints from target image. The nearest neighbor is the keypoint with minimum Euclidean distance for the invariant descriptor. All matches with distance ratio greater than 0.8 are rejected, thereby eliminating about 90% false matches and 5% correct matches. Best-Bin-First (BBF) [52] is an approximate nearest neighbor algorithm. It uses modified k-d tree which searches bins in the feature space in the order of their closest distance from query location. The heap-based priority queue is used for efficient

determination of the search order. An approximation is obtained by limiting search to the specific number of the nearest bins.

Finding homography using RANSAC

RANSAC, proposed by Fiscler and Bolles, is a method for deriving a mathematical model iteratively from a data set containing outliers [50]. It identifies the outliers in a data set and derives the relevant model using dataset without outliers. It filters out wrongly mapped points coming due to inaccuracies of the SIFT method. RANSAC classifies the matching features into inliers and outliers. The former are data points that hold on to the model while outliers do not. This is a non-deterministic method as reasonable result is produced only with a certain probability which increases with the number of iterations allowed. RANSAC accomplishes its goal with the following steps:

1. Randomly select a subset of the original data. This subset may be called hypothetical inliers
2. Selected hypothetical inliers are fitted to a model.
3. Remaining data are tested against the model. The points fitting to the derived model well based on loss functions are said to be part of consensus set.
4. Repetition of steps from 1 to 3 for a specified number of iterations (k).

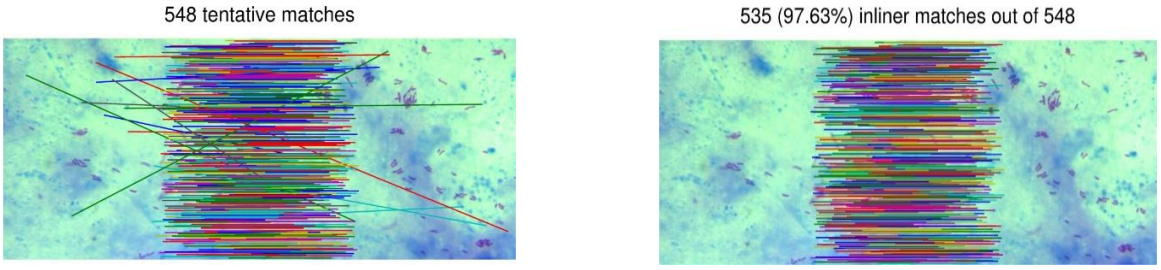

Figure 15. Left: Matching of two image sub parts, Right: Removal of outliers using RANSAC

The advantage with RANSAC is its ability to robustly estimate the model parameters with high accuracy even if the data has large number of outliers [50].

Computing Mosaic by combining subparts of view fields

The overlapping regions of the two images are blend together with equal weights to generate a mosaic. The following steps were implemented to generate mosaic by combining all the subparts:

NaN (not a number) removal

When images are stitched to produce a mosaic, the general problem encountered is the presence of large number of NaNs at the boundaries of the mosaic image. To solve this problem, NaN values were replaced by smooth interpolation [56].

B. Implementation of divide and conquer algorithm

Linear stitching of all the subparts of images is computationally intensive. The task was segregated into one row at a time strategy. Since the view field images of a ZN-stained slide are taken in rows and columns as can be seen in Figure 11, this would be an effective strategy. This algorithm was implemented in following steps:

i) Row stitching: All the subparts of an image in a row were stitched to produce mosaic A (Figure 16). Similarly, mosaic B was produced by stitching all subparts of an image of the next row.

Figure 16: Row stitching

ii) Row transformation: Mosaic A and B were rotated so that their horizontal overlapping regions (left: Figure 17) stitched vertically as in step i (right: Figure 17). The rotational transformation is done so that overlapping subparts come along the x-axis and both the mosaics are stitched together to produce a new mosaic C (Figure 17). The mosaic C will then serve as mosaic A for the next row and subsequent row mosaic will be combined to form a new mosaic.

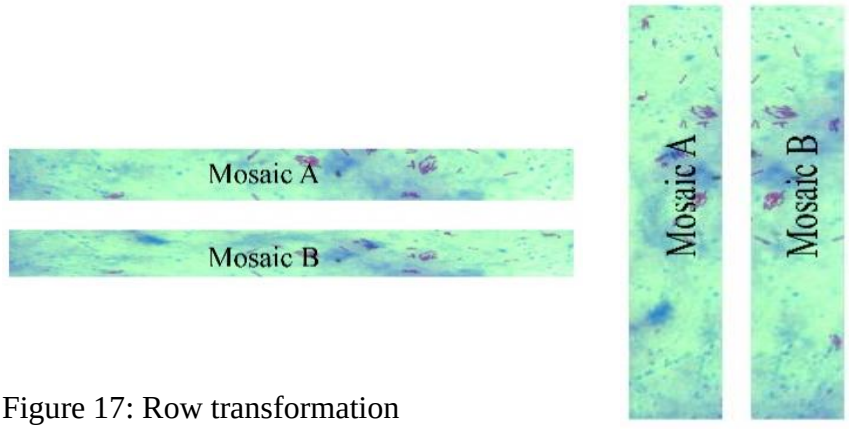

Figure 17: Row transformation

iii) Repeat the step ii till all the rows are stitched to produce a final mosaic.

iv) The final mosaic was transformed rotationally to correct rotational changes due to row transformation.

RESULTS AND DISCUSSIONS

The overlapping subparts of the view field image were stitched together into a mosaic using divide and conquer algorithm. The mosaic was then compared with the original view field image to validate the proposed methodology.

3.1. Conversion to grayscale

Conversion to individual channels leads to the transformation of a RGB color image to a grayscale image. The common method of converting RGB image to grayscale is to eliminate the Hue and saturation information and to retain only the luminance value of the image. As can be seen from Table 3, the number of matches is low as compared to number of matches obtained by first converting image to HSV and LAB colorspaces followed by separation into individual channels. The 'H', 'S', 'b' and 'a' channels provided better matches than the earlier methods [46]. The number of keypoint matches is highest for 'a' channel of the LAB colorspace (Table 3).

Table 3: Comparison of the number of matches obtained after stitching of datasets using various color channels.

Color Component	Number of matches (DA (P1))	Number of matches (DB (P1))
Value (V)	85318	85252
Saturation (S)	120244	118862
Hue (H)	112527	117548
B channel	113518	115240
A channel	123994	121312
Luminance (L)	94126	95935
Grayscale	101643	99771

3.2. Application of Divide and conquer algorithm

To reduce time of stitching, divide and conquer algorithm was implemented. The time for stitching was decreased significantly using this strategy as evident from Table 1. Failure in stitching of few view fields, and high dissimilarity between original and stitched images was noticed when linear stitching of subparts of images was performed. The parallel computing toolbox of the MATLAB was used for parallelizing the algorithm. The algorithm was modified to calculate the SIFT features in parallel. The number of cores on which the algorithm implemented was set to four. The time taken for stitching is reduced to almost half with the parallelization (Table 4). As the number of subparts is increased, the stitching time increases linearly for parallel, and divide and conquer methods while time required for stitching is significantly higher for linear stitching method. In former methods, time required in stitching is consistent for both datasets while inconsistency was observed in linear method (Table 4).

Table 4: Comparison of computational time for stitching using Matlab parallel toolbox, divide and conquer and linear stitching methods.

Dataset	Average time taken in seconds for stitching subparts of a view field image		
	Parallel method	Divide and conquer method	Linear method
DA (P1)	10.282	18.067	33.073
DB (P1)	10.535	18.286	33.464
DA (P2)	17.684	34.733	88.570
DB (P2)	18.232	35.335	111.141
DA (P3)	27.731	45.372	307.854
DB (P3)	28.172	45.910	159.168

*DA and DB represent Datasets A and B respectively. P1, P2 & P3 correspond to 2x2, 3x3 and 3x5 overlapping subparts of the view field image.

3.3 Validation

After formation of mosaic, the similarity between stitched and original images was compared to evaluate the effectiveness of the proposed method. Significantly high similarity scores were obtained between stitched and original images based on correlation and structural similarity (structural similarity (SSIM) and feature-similarity (FSIM)) indexes (Table 5). Comparable values of similarity among different subpart types are obtained using divide and conquer method signify the consistency of proposed method. The SSIM index is used for measuring the similarity between two images and is based on the idea that human visual system is highly adapted to process structural information [53]. FSIM index is computed by generating a single similarity score by grouping the similarity maps [54]. Correlation, r is used to measure similarity between two aligned images.

Comparison with other tools

The proposed method is compared with robust software Autostitch and MicroMos used for image stitching. Our stitching results were found to be significantly better than both Autostitch and MicroMos software as can be inferred from visual inspection (Figure 18) and image similarity scores (Table 5).

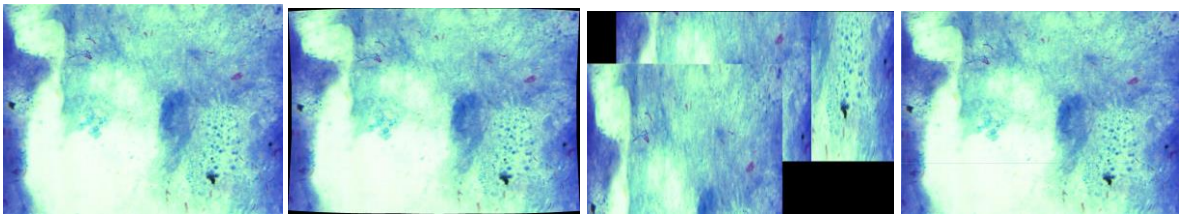

(a) (b) (c) (d)

Figure 18: Comparison between original view field images with stitched mosaics. Original image (a), mosaic formed using Autostitch (b), MicroMos (c) and the current method (d).

The development of a CAD system for automated grading of the sputum smear slide requires the view fields to be focused, stitching of view fields into a single image, and subsequently counting of the bacilli in an automated manner. If the CAD-assisted smear slide TB detection method equals or exceeds the performance of an experienced microscopist then it would reduce the number of patients requiring Xpert MTB/RIF or culture tests. As good result for automated stitching was obtained, the final mosaic can be used for grading the slide. The process of autostitching would thereby reduce error in grading due to duplicate bacilli found in overlapping regions. Parallelization and divide and conquer algorithms can significantly reduce the amount of time required to stitch the view fields.

Table 5. Similarity scores obtained by comparison between the stitched and original images

DATASET							
Methodology	Similarity Measure	*DA(P1)	*DB(P1)	*DA(P2)	*DB(P2)	*DA(P3)	*DB(P3)
Divide and Conquer method	COR*	0.997	0.996	0.997	0.996	0.995	0.991
	SSIM	0.988	0.990	0.988	0.989	0.969	0.969
	FSIM	0.989	0.991	0.990	0.991	0.976	0.976
Linear Method	COR*	0.982	0.896	0.742	0.828	0.575	0.789
	SSIM	0.962	0.943	0.817	0.898	0.699	0.857
	FSIM	0.966	0.943	0.839	0.907	0.729	0.876
Autostitch	COR*	0.847	0.751	0.995	0.959	0.913	0.973
	SSIM	0.93	0.946	0.995	0.974	0.779	0.984
	FSIM	0.92	0.922	0.983	0.956	0.826	0.969
MicroMos	COR*	0.814	0.736	0.157	0.109	0.126	0.088
	SSIM	0.858	0.856	0.308	0.362	0.324	0.387
	FSIM	0.925	0.924	0.673	0.696	0.678	0.700

*COR stands for correlation. DA and DB represent Datasets A and B respectively. P1, P2 & P3 correspond to 2x2, 3x3 and 3x5 overlapping subparts of the view field image.

Due to its cost effectiveness, ZN-stained sputum smear microscopy is the most common method for diagnosis of TB. Although culture tests and Expert MTB/RIF have better accuracy, they are available only in highly specialized laboratories and are not available in diagnostic centres of hospitals dealing TB patients. Since autostitching is the critical step in

autograding of ZN-stained sputum smear slides, the proposed method would assist in the automated diagnosis of TB using ZN-stained sputum smear microscopy. The proposed methodology was validated on the overlapping subparts of the view field image to mimic the uniformly focused overlapping view fields obtained from a motorized microscope. Since efficient methods for autofocusing and identification of bacilli in a view field have already been developed, combination of our method with autofocusing and bacilli identification techniques would lead to development of a microscopy system similar to TBDx, which grades fluorescent TB sputum smear slides automatically.

CONCLUSIONS

The CAD methods for better TB detection have developed using both CXRs and ZN-stained smear microscopy. These methods provide second opinion to clinicians for their findings, so their implementation is expected to improve the performance in diagnosis of TB. Features extracted by methods such as Gabor, Gist, HOG, and PHOG enabled SVM to efficiently discriminate between the TB and non-TB CXR images. Validations of results using five-fold cross-validation and independent datasets have shown that the performance of these features is significantly higher than that of textural features. CAD techniques proposed earlier were mainly based on the segmentation of CXRs followed by the extraction of GLCM textural features. The major limitation with these methods is that they cannot be incorporated into existing X-ray machines for automated detection of TB due to their dependency on manual or semi-automated segmentation. Although GLCM textural features extracted from the automatically segmented CXRs can be used for automated detection, however, the performance of this method is exceedingly poor. Since the features (Gabor, Gist, HOG, and PHOG) extracted from the whole CXR do not require region of interest identification using segmentation, these features can easily be implemented to existing digital X-ray machines for the automated TB detection. As Gist and PHOG features provided the best discrimination between the non-TB and TB for both 8-bit and 14-bit CXRs, these features were used to develop a MATLAB toolbox, TB-Xpredict, which can effortlessly train as well as predict CXRs as TB or non-TB. TB-Xpredict has a very simple GUI for automated training and classification of CXRs, and requires only basic knowledge of computer to operate.

ZN-stained sputum smear microscopy is an essential step in the diagnosis of TB according to the guidelines of the WHO. Its accuracy is highly variable due to expertise of the microscopist, and various human errors. Automation for grading of bacilli is highly desired to

reduce human errors as well as mass screening of smear slides. Automation requires execution of loading of slides, focusing, stitching and counting of bacilli in an automated manner. The current work outlined and implemented a method for automated stitching of view fields. To validate the method, the view field images were cropped into different overlapping subparts of equal sizes, so as to mimic the images obtained from an automated motorized microscope. The 'a' channel of the CIELAB colorspace provided the best result. SIFT features were used for feature detection and extraction, and RANSAC was used for removing outlier. The subparts of the image were then stitched using divide and conquer algorithm. This method not only decreased the time complexity of the method but also provided significantly better stitching results compared to linear stitching. The validation was done through similarity measure between the stitched and the original image both visually and quantitatively. Most of the microscopy slides are acquired in this fashion; therefore, this methodology can be extended for stitching of view fields of other histopathological microscopy tests.

A hybrid system (concept for design of a new instrument) resulting from the combination of outcomes from CXRs and ZN-stained smear microscopy would lead to significant increase in the sensitivity and accuracy of TB detection. The system would also reduce work load, time taken for reporting results and human errors. This system can effectively be used for mass screening of TB in high burden settings particularly in HIV endemic areas.

References

1. WHO. (2014). Global Tuberculosis Report 2014. World Health Organization. Chicago.

2. World Health Organization. (2010). Treatment of tuberculosis: guidelines. World Health Organization.

3. Veropoulos, K., Learmonth, G., Campbell, C., Knight, B., and Simpson, J. (1999). Automated identification of tubercle bacilli in sputum. A preliminary investigation. Analytical and quantitative cytology and histology/the International Academy of Cytology [and] American Society of Cytology, 21(4), 277-282.

4. Noble, M., Bruening, W., Uhl, S., and Schoelles, K. (2009). Computer-aided detection mammography for breast cancer screening: systematic review and meta-analysis. Archives of gynecology and obstetrics, 279(6), 881-890.

5. Gur, D., Sumkin, J. H., Rockette, H. E., Ganott, M., Hakim, C., Hardesty, L., and Wallace, L. (2004). Changes in breast cancer detection and mammography recall rates

after the introduction of a computer-aided detection system. Journal of the National Cancer Institute, 96(3), 185-190.

6. Doi, K. (2007). Computer-aided diagnosis in medical imaging: historical review, current status and future potential. Computerized medical imaging and graphics, 31(4), 198-211.

7. Dean, J. C., and Ilvento, C. C. (2006). Improved cancer detection using computer-aided detection with diagnostic and screening mammography: prospective study of 104 cancers. American Journal of Roentgenology, 187(1), 20-28.

8. Breuninger, M., van Ginneken, B., Philipsen, R. H., Mhimbira, F., Hella, J. J., Lwilla, F., and Reither, K. (2014). Diagnostic accuracy of computer-aided detection of pulmonary tuberculosis in chest radiographs: a validation study from sub-saharan Africa.

9. Somoskövi, A., Györi, Z., Czoboly, N., and Magyar, P. (1999). Application of a computer-directed automated microscope in mycobacteriology [Technical Note]. The International Journal of Tuberculosis and Lung Disease, 3(4), 354-357.

10. Haralick, R. M., Shanmugam, K., and Dinstein, I. H. (1973). Textural features for image classification. Systems, Man and Cybernetics, IEEE Transactions on, (6), 610-621.

11. Van Ginneken, B., Katsuragawa, S., ter Haar Romeny, B. M., & Viergever, M. (2002). Automatic detection of abnormalities in chest radiographs using local texture analysis. Medical Imaging, IEEE Transactions on, 21(2), 139-149.

12. Hogeweg, L., Mol, C., de Jong, P. A., Dawson, R., Ayles, H., and van Ginneken, B. (2010). Fusion of local and global detection systems to detect tuberculosis in chest radiographs. In Medical Image Computing and Computer-Assisted Intervention–MICCAI 2010 (pp. 650-657). Springer Berlin Heidelberg.

13. Tan, J. H., Acharya, U. R., Tan, C., Abraham, K. T., and Lim, C. M. (2012). Computer-assisted diagnosis of tuberculosis: a first order statistical approach to chest radiograph. Journal of medical systems, 36(5), 2751-2759.

14. Arzhaeva, Y., Hogeweg, L., de Jong, P. A., Viergever, M. A., and van Ginneken, B. (2009). Global and local multi-valued dissimilarity-based classification: Application to computer-aided detection of tuberculosis. In Medical Image Computing and Computer-Assisted Intervention–MICCAI 2009 (pp. 724-731). Springer Berlin Heidelberg.

15. Arzhaeva, Y., Tax, D. M., and van Ginneken, B. (2009). Dissimilarity-based classification in the absence of local ground truth: Application to the diagnostic interpretation of chest radiographs. Pattern Recognition, 42(9), 1768-1776.

16. Shen, R., Cheng, I., and Basu, A. (2010). A hybrid knowledge-guided detection technique for screening of infectious pulmonary tuberculosis from chest radiographs. Biomedical Engineering, IEEE Transactions on, 57(11), 2646-2656.

17. Oliva, A., and Torralba, A. (2001). Modeling the shape of the scene: A holistic representation of the spatial envelope. International journal of computer vision, 42(3), 145-175.

18. Manjunath, B. S., and Ma, W. Y. (1996). Texture features for browsing and retrieval of image data. Pattern Analysis and Machine Intelligence, IEEE Transactions on, 18(8), 837-842.

19. Dalal, N., and Triggs, B. (2005, June). Histograms of oriented gradients for human detection. In Computer Vision and Pattern Recognition, 2005. CVPR 2005. IEEE Computer Society Conference on (Vol. 1, pp. 886-893). IEEE.

20. Bosch, A., Zisserman, A., and Munoz, X. (2007, July). Representing shape with a spatial pyramid kernel. In Proceedings of the 6th ACM international conference on Image and video retrieval (pp. 401-408). ACM.

21. Abràmoff, M. D., Magalhães, P. J., and Ram, S. J. (2004). Image processing with ImageJ. Biophotonics international, 11(7), 36-42.

22. Chan, T. F., Sandberg, B. Y., and Vese, L. A. (2000). Active contours without edges for vector-valued images. Journal of Visual Communication and Image Representation, 11(2), 130-141.

23. Wong, L. P., & Ewe, H. T. (2005, January). A study of lung cancer detection using chest x-ray images. In Proceedings of 3rd APT Telemedicine Workshop, Kuala Lumpur (pp. 27-28).

24. Luisier, F., Blu, T., and Unser, M. (2007). A new SURE approach to image denoising: Interscale orthonormal wavelet thresholding. Image Processing, IEEE Transactions on, 16(3), 593-606.

25. Grigorescu, S. E., Petkov, N., and Kruizinga, P. (2002). Comparison of texture features based on Gabor filters. Image Processing, IEEE Transactions on, 11(10), 1160-1167.

26. Yang, Y., and Newsam, S. (2008, October). Comparing SIFT descriptors and Gabor texture features for classification of remote sensed imagery. In Image Processing, 2008. ICIP 2008. 15th IEEE International Conference on (pp. 1852-1855). IEEE.

27. Oliva, A., and Torralba, A. (2006). Building the gist of a scene: The role of global image features in recognition. Progress in brain research, 155, 23-36.

28. Siagian, C., and Itti, L. (2007). Rapid biologically-inspired scene classification using features shared with visual attention. Pattern Analysis and Machine Intelligence, IEEE Transactions on, 29(2), 300-312.

29. Junior, O. L., Delgado, D., Gonçalves, V., and Nunes, U. (2009, October). Trainable classifier-fusion schemes: an application to pedestrian detection. In Intelligent Transportation Systems (Vol. 2).

30. Hall, M., Frank, E., Holmes, G., Pfahringer, B., Reutemann, P., and Witten, I. H. (2009). The WEKA data mining software: an update. ACM SIGKDD explorations newsletter, 11(1), 10-18.

31. Cortes, C., and Vapnik, V. (1995). Support-vector networks. Machine learning, 20(3), 273-297.

32. Chang, C. C., and Lin, C. J. (2011). LIBSVM: A library for support vector machines. ACM Transactions on Intelligent Systems and Technology (TIST), 2(3), 27.

33. Metz, C. E. (1978, October). Basic principles of ROC analysis. In Seminars in nuclear medicine (Vol. 8, No. 4, pp. 283-298). WB Saunders.

34. Robin, X., Turck, N., Hainard, A., Tiberti, N., Lisacek, F., Sanchez, J. C., and Müller, M. (2011). pROC: an open-source package for R and S+ to analyze and compare ROC curves. BMC bioinformatics, 12(1), 77.

35. DeLong, E. R., DeLong, D. M., and Clarke-Pearson, D. L. (1988). Comparing the areas under two or more correlated receiver operating characteristic curves: a nonparametric approach. Biometrics, 837-845.

36. Lewis, J. J., Chihota, V. N., Van der Meulen, M., Fourie, P. B., Fielding, K. L., Grant, A. D., and Churchyard, G. J. (2012). "Proof-Of-Concept" Evaluation of an Automated Sputum Smear Microscopy System for Tuberculosis Diagnosis.

37. Sadaphal, P., Rao, J., Comstock, G. W., and Beg, M. F. (2008). Image processing techniques for identifying Mycobacterium tuberculosis in Ziehl-Neelsen stains [Short Communication]. The International Journal of Tuberculosis and Lung Disease, 12(5), 579-582.

38. Khutlang, R., Krishnan, S., Whitelaw, A., and Douglas, T. S. (2010). Automated detection of tuberculosis in Ziehl-Neelsen-stained sputum smears using two one-class classifiers. Journal of microscopy, 237(1), 96-102.

39. Forero-Vargas, M. G., Sroubek, F., Alvarez-Borrego, J., Malpica, N., Cristóbal, G., Santos, A., and Cohen, L. (2002, November). Segmentation, autofocusing and signagture extraction of tuberculosis sputum images. In International Symposium on Optical Science and Technology (pp. 171-182). International Society for Optics and Photonics.

40. Mateos-Pérez, J. M., Redondo, R., Nava, R., Valdiviezo, J. C., Cristóbal, G., Escalante-Ramírez, B., and Desco, M. (2012). Comparative evaluation of autofocus algorithms for a real-time system for automatic detection of Mycobacterium tuberculosis. Cytometry Part A, 81(3), 213-221.

41. Russell, M. J., and Douglas, T. S. (2007, August). Evaluation of autofocus algorithms for tuberculosis microscopy. In Engineering in Medicine and Biology Society, 2007. EMBS 2007. 29th Annual International Conference of the IEEE (pp. 3489-3492). IEEE.

42. Costa Filho, C. F., Costa, M. G. F., and Kimura Junior, A. (2012). Autofocus functions for tuberculosis diagnosis with conventional sputum smear microscopy. Current Microscopy Contributions to Advances in Science and Technology. Badajoz: Formatex, 13-20.

43. Subramanyam, M. V. (2012, December). Automatic image mosaic system using steerable Harris corner detector. In Machine Vision and Image Processing (MVIP), 2012 International Conference on (pp. 87-91). IEEE.

44. Bai, X., Ning, X., and Wang, L. (2012, July). Analysis and comparison of feature detection and matching algorithms for rovers vision navigation. In Instrumentation and Control Technology (ISICT), 2012 8th IEEE International Symposium on (pp. 66-71). IEEE.

45. Ali, S., and Hussain, M. (2012, December). Panoramic image construction using feature based registration methods. In Multitopic Conference (INMIC), 2012 15th International (pp. 209-214). IEEE.

46. Brown, M., and Lowe, D. G. (2007). Automatic panoramic image stitching using invariant features. International journal of computer vision, 74(1), 59-73.

47. Yongwei, M., Xinke, G., Xianjun, D., and Jiayin, X. (2009, June). A New Method of Microscopic Images' Automatic Mosaicing. In Bioinformatics and Biomedical Engineering, 2009. ICBBE 2009. 3rd International Conference on (pp. 1-5). IEEE.

48. Piccinini, F., Bevilacqua, A., and Lucarelli, E. (2013). Automated image mosaics by non-automated light microscopes: the MicroMos software tool. Journal of microscopy, 252(3), 226-250.

49. Lowe, D. G. (2004). Distinctive image features from scale-invariant keypoints. International journal of computer vision, 60(2), 91-110.

50. Fischler, M. A., and Bolles, R. C. (1981). Random sample consensus: a paradigm for model fitting with applications to image analysis and automated cartography. Communications of the ACM, 24(6), 381-395.

51. Panchal, P. M., Panchal, S. R., and Shah, S. K. (2013). A comparison of SIFT and SURF. International Journal of Innovative Research in Computer and Communication Engineering, 1(2), 323-327.

52. Beis, J. S., and Lowe, D. G. (1997, June). Shape indexing using approximate nearest-neighbour search in high-dimensional spaces. In Computer Vision and Pattern Recognition, 1997. Proceedings., 1997 IEEE Computer Society Conference on (pp. 1000-1006). IEEE.

53. Wang, Z., Simoncelli, E. P., and Bovik, A. C. (2003, November). Multiscale structural similarity for image quality assessment. In Signals, Systems and Computers, 2004. Conference Record of the Thirty-Seventh Asilomar Conference on (Vol. 2, pp. 1398-1402). IEEE.

54. Zhang, L., Zhang, L., Mou, X., and Zhang, D. (2011). FSIM: a feature similarity index for image quality assessment. Image Processing, IEEE Transactions on, 20(8), 2378-2386.

55. Patel, B., and Douglas, T. S. (2011, August). Creating a virtual slide map of sputum smears by auto-stitching. In Engineering in Medicine and Biology Society, EMBC, 2011 Annual International Conference of the IEEE (pp. 5088-5091). IEEE.

56. d'Errico, J. (2004). Inpaint nans. MATLAB Central File Exchange.

List of publications

Patent:

1. Rout C, Chauhan A, Chauhan RS and Chauhan D (2013) "Automated Computer Aided Diagnosis (CAD) of Tuberculosis using Chest X-Ray (Journal No. 35/2014, Publication date: 29/08/2014).

Journal:

1. Chauhan A, Chauhan D and Rout C and (2014), "Role of Gist and PHOG features in computer-aided diagnosis of tuberculosis without segmentation". PLoS ONE, 9(11): e112980. doi:10.1371/journal.pone.0112980 (IF=3.3)

2. Chauhan A, Sarkar M, Gupta P and Rout C (2015), "Automated stitching of view fields of ZN-stained sputum smear microscopy slides", Journal of Information Processing Systems"(Accepted).

Conference:

1. Chauhan A, Chauhan D, and Rout C, Automatic Classification of Chest X-rays using Histogram of Gradients. Indian Conference on Medical Informatics and Telemedicine, ICMIT 2013, IIT, Kharagpur, 28 - 30 March, 2013.

2. Mishra S, Shah MI, Sarkar M, Chauhan A, Sharma S, Rout C (2014). Integration of medical data for affordable healthcare. Proceedings of the International Conference on Data Sharing and Integration for Global Sustainability [New Delhi, India: 2nd - 5th November, 2014].